MNE 23 (2024) 100241

Contents lists available at ScienceDirect

Micro and Nano Engineering

journal homepage: www.sciencedirect.com/journal/micro-and-nano-engineering

Design and fabrication of an opto-mechanical antenna in the NIR range

Daniyal Khosh Maram [a,*], Xavier Borrisé [b], Joan Garcia-Garcia [a], Raul Ruiz [a], Xavier Cartoixà [a], Gabriel Abadal [a]

[a] Departament d'Enginyeria Electrònica, Universitat Autònoma de Barcelona, 08193 Bellaterra, Barcelona, Spain
[b] Catalan Institute of Nanoscience and Nanotechnology (ICN2) and Barcelona Institute of Science and Technology (BIST), Barcelona, Spain

ARTICLE INFO

Keywords:
Opto-mechanical antenna
NIR optical detector
Plasmonic optical nanoantenna
MEMS/NEMS resonators

ABSTRACT

In this study we present a novel device for the direct transduction of optical radiation in the near-infrared region into mechanical actuation, which is based on a plasmonic optical nanoantenna integrated in a microcantilever. We propose and demonstrate the feasibility of a simple fabrication process consisting in the nano-tailoring of a commercially available Atomic Force Microscope (AFM) cantilever by means of the Focused Ion Beam (FIB) milling technique. Furthermore, the comprehensive analysis of the device performance characteristics included in this work reveals the different sensitivity values of these characteristics to the fabrication process tolerances of the most relevant geometric design parameters.

1. Introduction

The concept of MEMSTENNA, a term derived from MEMS (Micro-Electro-Mechanical Systems) and antenna introduced in previous works by R. Ruiz et al. [1–3], has demonstrated to enable direct transduction from the electromagnetic domain in the radiofrequency range to the mechanical domain, within the feed-gap of radiofrequency antenna structures. In such MEMSTENNA devices, both static and dynamic actuation is remotely achieved, so that capacitive MEMS structures are mechanically excited without any reliance on a local power supply. An extension of the MEMSTENNA concept to the 1–10 THz frequency range was proposed previously by C. Belacel et al. [4] as a novel THz detector, whose operating principle is also based on the direct transduction from the electromagnetic domain to the mechanical domain. Unlike other THz bolometric detectors based on MEMS structures, such as clamped-clamped beam resonators [5], clamped-free beams with an absorbing metasurface [6] or clamped-clamped beams driven by dielectric forces [7], direct transduction allows to enhance the THz detector frequency response at room temperature, since thermal domain is not present in the transduction mechanism. Other examples of electromagnetic to mechanical direct transduction are found in the optical range. In cavity optomechanical systems, for instance, direct light matter interaction, which is in the basis of atom cooling foundational works [8], is used to amplify to the self-sustained level or to cool-down to the ground state the vibrations of a mechanical oscillator [9]. In most of the cases, cavity optomechanical devices consist of Fabry-Perot interferometers built using highly reflective MEMS membranes [10], but more complex structures such as wine glass mode NEMS resonators [11] or suspended photonic crystals [12] have demonstrated to show quantum effects related to photon-phonon interaction.

On the other hand, optical nanoantenna technology [13,14] emerged as a promising alternative to semiconductor detectors [15] and photovoltaic energy harvesting transducers [16–18]. However, here again, slow time constants of the thermal mechanisms involved in bolometric detection schemes [19] limits the frequency response of these optical nanoantenna detectors, and optical rectenna configurations based on the combination of an optical nanoantenna and a fast integrated rectifier are limited by the impedance mismatch of the antenna and the diode rectifier [20].

In the present study, we propose to extend the MEMSTENNA concept to the near-infrared (NIR) optical frequency range, in order to keep the advantage of direct transduction in terms of frequency response [1–3], namely to get a faster response of the device and a wider frequency bandwidth than traditional bolometric based detector of radiation, which are based in a slow opto-thermally induced mechanical actuation effect. We name the novel device with the new term NEMSTENNA, denoting the fusion in this case of a plasmonic optical nanoantenna [21] with a MEMS structure. A NIR NEMSTENNA has applications beyond the optical sensors field as the fast transducer of a wide bandwidth NIR detector, in, for instance, the actuators area. Here, for example, the NIR

* Corresponding author.
E-mail address: daniyal.khoshmaram@uab.cat (D.K. Maram).

https://doi.org/10.1016/j.mne.2024.100241
Received 17 November 2023; Received in revised form 23 February 2024; Accepted 2 March 2024
Available online 4 March 2024

NEMSTENNA can be used as the basic element of a nano-switch or a nano-relay actuated remotely by a NIR control signal. Since the IR radiation can be used as the control switch-on and switch-off signal but at the same time as the power means, NEMSTENNA would enable a wireless and batteryless switch/relay nanodevice. A switch/relay with these characteristics can benefit by its reduced dimensions and power autonomy to be integrated, for instance, in implanted microsystems where the use of batteries becomes an issue. In following, this study has been outlined. In section 2, we present the NEMSTENNA device layout and the transduction mechanisms involved in the operation principle. Section 3 covers the fabrication process and presents results concerning the geometry characterization of the fabricated structures. In Section 4, we delve into a sensitivity analysis of both S_{11} resonance and gap induced voltage vs. frequency conducted using COMSOL, along with discussions on NEMSTENNA deflection and gap voltage induction within varying gap distances.

2. Device structure and working principle

2.1. Opto-mechanical antenna structure

Our proposed device structure consists of a NIR optical dipole nanoantenna ($\lambda = 1.55$ μm) integrated in one of the metal sides of the free-end of two Au-coated silicon nitride triangular microcantilevers, as shown in Fig. 1. The dipole nanoantenna geometry is defined by its two components' length and width (L_1, L_2, W_1) as well as the dimensions of the supporting arms (L_{Arm1}, L_{Arm2}, W_2) which connect the dipole components to the microcantilevers. Notice that the cross shape is a geometry that allows to define the dipole in one direction (the polarization direction of the IR linearly polarized beam) and the supporting arms connected to the dipole in the feed-gap area in the perpendicular direction, in order not to interfere the dipole behaviour. The Si_3N_4 thickness in the nanoantenna area is also considered as a design parameter. Both components of the nanoantenna are parallelly placed at a gap distance in an overlap area in the feed region of the antenna, defining a transduction capacitance that will electrically load the nanoantenna (Fig. 1).

2.2. Opto-mechanical antenna working principle

The working principle of the opto-mechanical antenna hinges upon a well-defined transduction chain. Specifically, when the nanoantenna is exposed to a resonant radiation source (a NIR laser with $\lambda_{NIR} = 1.55$ μm –$f_{NIR} = 193.41$ THz–, for instance), a voltage denoted as V_{gap} is induced within the feed gap region of the antenna. This induced voltage stems from the interaction between the incident radiation and the plasmonic optical nanoantenna, and is an ac voltage with the same frequency of the exciting radiation ($f_{NIR} = 193.41$ THz), as described by the following equation:

$$V_{gap} = V_0 \cdot sin(\omega_{NIR} t) \tag{1}$$

Using Eq. (2) [22,23], we can calculate V_{gap} from the electric field in the feed gap region by the integration of this electric field E along the gap distance.

$$V_{gap} = -\int_{gap} \vec{E} \cdot d\vec{l} \tag{2}$$

Subsequently, this voltage V_{gap} will induce an electrostatic force. This force will be applied at both components of the nanoantenna dipole in the gap region and, eventually, it will produce their mutual attraction (see Fig. 2). Remarkably, this electrostatic force exhibits a nonlinear relationship with the voltage V_{gap} as shown in Eq. (3) [2]:

$$F_{ee} = \frac{\varepsilon_0 A V_{gap}^2}{2\,(g_0 - z_1 - z_2)^2}, \tag{3}$$

where A is overlapping area, ε_0 is the air dielectric constant, V_{gap} is the

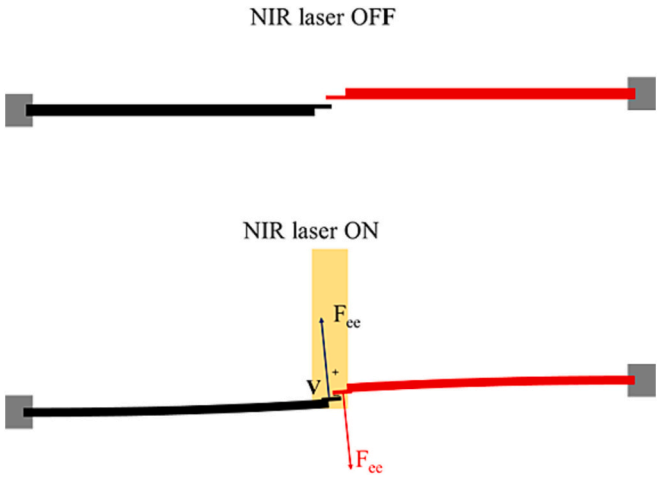

Fig. 2. Actuation principle of the opto-mechanical antenna.

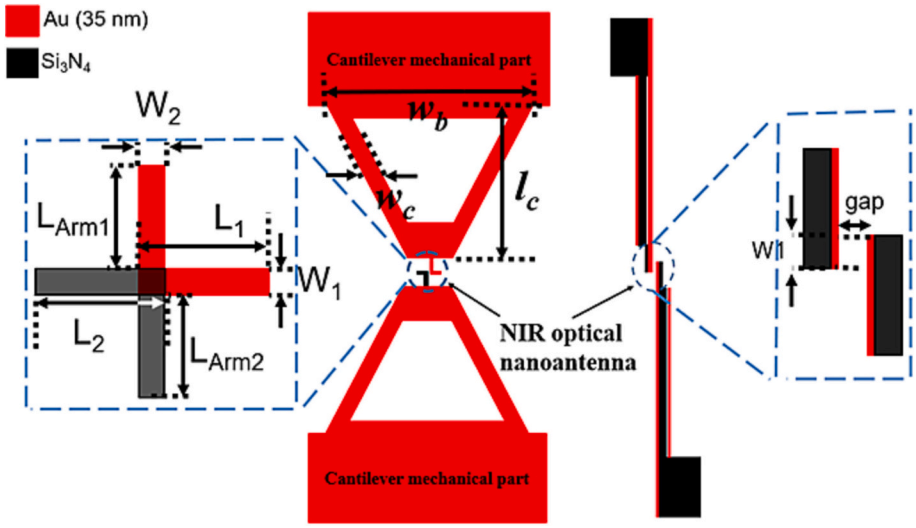

Fig. 1. Schematic top and side views of the proposed structure including nano-antenna and microcantilever.

induced voltage within the gap area, g_0 is the gap distance, z_1 and z_2 are the deflections of each one of the beams and F_{ee} is the electrostatic force. This nonlinearity leads to the emergence of a DC component of the force, which can be obtained by combining Eqs. (1) and (3):

$$F_{ee} = \frac{\epsilon_0 A}{2(g_0 - z_1 - z_2)^2} \cdot (V_0 sin(\omega_{NIR} t))^2 = \frac{\epsilon_0 A V_0^2}{2(g_0 - z_1 - z_2)^2} \cdot \left[\frac{1}{2} - \frac{1}{2} cos(2\omega_{NIR} t)\right] \quad (4)$$

Thus, the first term in the right side of Eq. (4) corresponds to the DC component of the force:

$$F_{ee,DC} = \frac{\epsilon_0 A V_0^2}{4(g_0 - z_1 - z_2)^2} \quad (5)$$

This resultant DC component of the electrostatic force is applied within the overlap region of the antenna structure and consequently it also induces a mutual attraction between both microcantilevers at their free ends, since they are mechanically attached to the nanoantenna through the connection arms.

The second term in the right side of Eq. (4) corresponds to an ac component of the force at a frequency twice the radiation frequency ($2 \cdot \omega_{NIR}$), that will not induce any significant mechanical vibration on the microcantilevers, since both the excitation force (hundreds of THz) and the natural vibration frequency (tenths of kHz) of the microcantilevers are orders of magnitude different.

3. Fabrication process

The fabrication process of the optical nanoantenna is carried out on the free end of tipless Atomic Force Microscope (AFM) microcantilevers, which are commercially available [24]. These cantilevers, characterized by their triangular geometry, as shown in (Fig. 1 and 3a), serve as the fundamental starting point for the subsequent nanoantenna integration. The structural material is 600 nm thick silicon nitride (Si_3N_4) with a 70/35 (top/bottom) nm thick Cr/Au coating layer. The V-shape structure is geometrically defined (Fig. 1) by the base width, w_b, arm length, l_c and arm width, w_c, and is supported by a Pyrex anchor. Nominal resonance frequency and spring constant are 17 kHz and 0.08 N/m respectively. After turning upside down the microcantilever (Fig. 3.b), the first step involves the local removal of the 70 nm Cr/Au layer and the subsequent thickness reduction of the silicon nitride (Si_3N_4) layer in a limited area at the free end of the cantilevers (Fig. 3c), by means of the FIB (Focused Ion Beam) milling nanolithography. In this first FIB step, the ion beam is scanned using a low Ga^+ beam current (700 pA) and a fast scan speed (1 s/scan) to avoid the redeposition of material and get a sort of brushing effect on the cantilever surface. A systematic calibration of the etch rate in previous conditions gives a value of around 33 nm/min which is translated to a resolution of the Si_3N_4 vertical etching process of 5–10 nm. However, as Si_3N_4 thickness is reduced below 50 nm, the structure starts to be unstable and bending collapse is finally produced, probably due to residual stress of the Au layer. So, 50 nm is a reliable lower limit of the Si_3N_4 thickness. After that, FIB milling is also employed to precisely define the structure of one of the nanoantenna's components. This is achieved through the complete removal of both the Si_3N_4 layer and the underlying bottom 35 nm thick Cr/Au layer (Fig. 3d). In this second

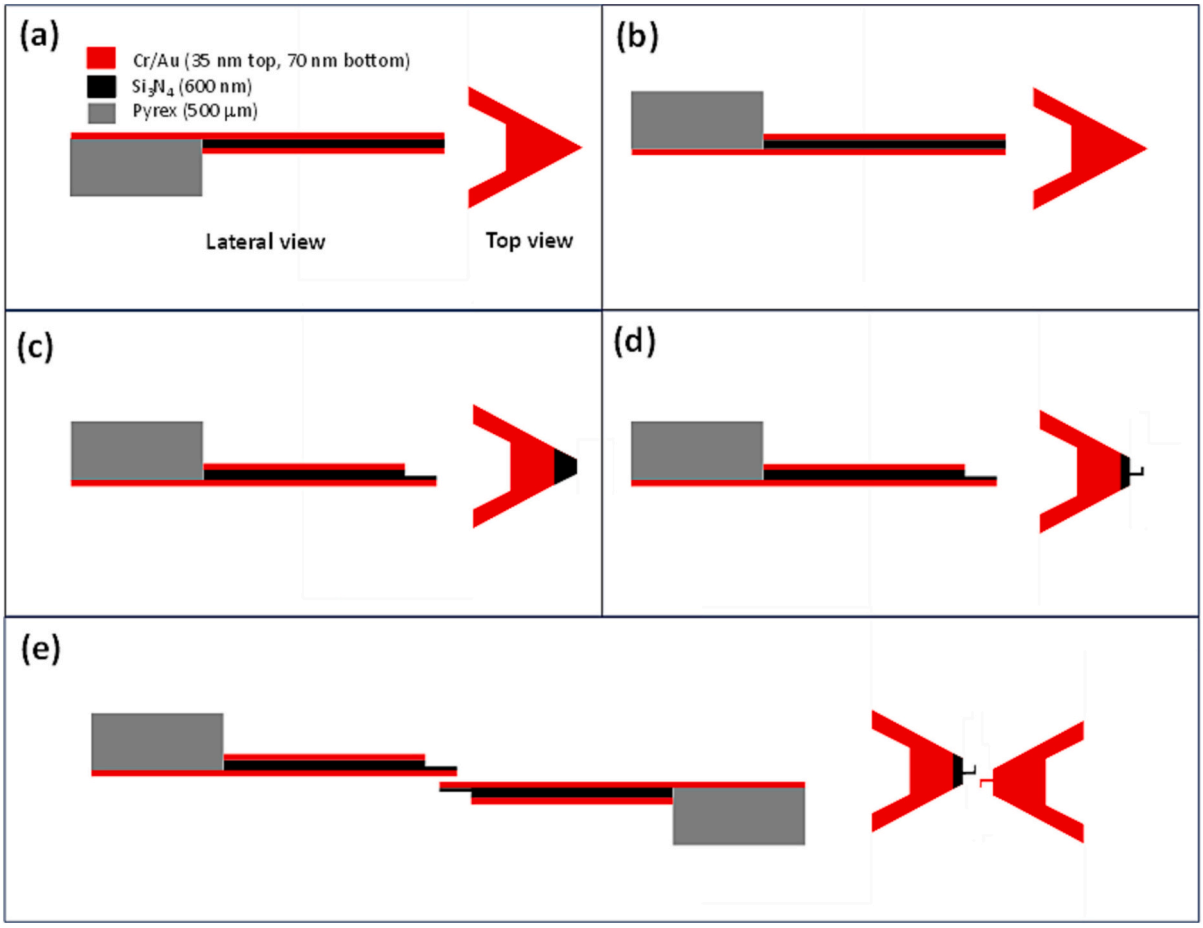

Fig. 3. FIB based fabrication process steps of the proposed structure: (a) Initial AFM microcantilever structure, (b) microcantilever flipping, (c) local FIB milling thickness reduction, (d) local FIB milling half nanoantenna definition and (e) NEMSTENNA final build-up.

FIB step, higher beam currents (3 nA) and slower scan speeds (10 s/scan) are used to enhance the etching throughput. However, in this case, these values, together with the beam aperture, are progressively reduced in order to increase the lateral etching resolution as we approach the final lateral dimensions of the antenna structure. In standard conditions, the fabrication tolerance associated to the lateral milling resolution would be around 10–20 nm. However, this value is increased to a maximum level of 50 nm due to lateral drifts and fluctuations of the suspended cantilever structure which is subjected to the charging effects of the Si_3N_4 layer. Alternative nanofabrication techniques as e-beam lithography (EBL), that would tighten the fabrication tolerance to 10 nm or below, would only be applicable if the antenna fabrication steps were included in the whole cantilever fabrication process.

FIB process implies an approximately 2 μm reduction in the cantilever length, translating into a 1% length reduction in this case, which consequently produces an increase of 2.8% in the spring constant and 1.8% in the resonance frequency. This process is repeated to define the second nanoantenna component in the very end of a second AFM microcantilever. Once the two components of the NEMSTENNA have been fabricated, one of them is flipped upside down and both are carefully placed, each bearing its nanostructured tip, in close proximity to each other (Fig. 3e) to complete the nanodipole antenna of the NEMSTENNA device. SEM images of Fig. 4 show the structural details and dimensions of a fabricated prototype of NEMSTENNA along its fabrication process described above. In particular, the transformation of the AFM microcantilever free end after silicon nitride thickness reduction (Fig. 4.a, corresponding to step c in Fig. 3), as well as the half nanoantenna definition (Fig. 4.b, corresponding to step d in Fig. 3) are shown.

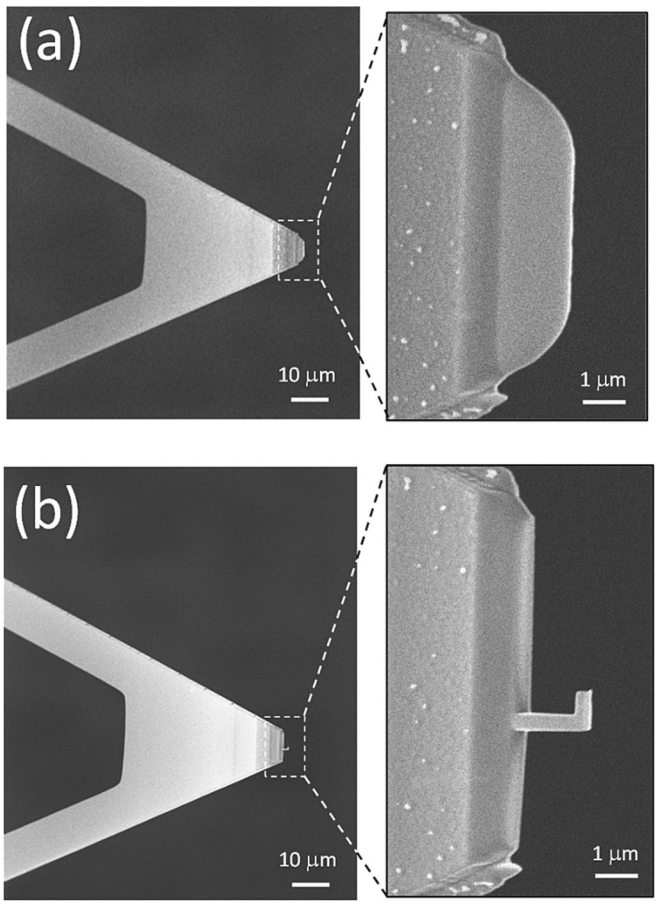

Fig. 4. SEM images of a fabricated NEMSTENNA prototype after (a) step c (see Fig. 3.c) and (b) step d (see Fig. 3.d) of the fabrication process.

4. Results and discussion

4.1. Simulation conditions

After demonstrating the fabrication of a NEMSTENNA structure, we have carried out an optimization process to tune the nanoantenna to the $\lambda = 1.55$ μm wavelength. Besides, we have performed a detailed sensitivity analysis of the most important NEMSTENNA characteristics to the dispersion of the fabrication parameters, to elucidate which are the most critical parameters that could mainly affect the performance of future fabricated devices.

To obtain a good prediction of the transduction response of the NEMSTENNA needed to optimize its performance and analyse its sensitivity to the fabrication tolerances, we have modelled and simulated the NEMSTENNA using COMSOL multiphysics simulation setup. Specifically, to follow the phenomenological sequence described in section 2.2, we have first modelled and simulated the optical nanoantenna part of the NEMSTENNA by means of the COMSOL multiphysics RF module to obtain, among other parameters, the nanoantenna voltage in the feedgap, V_{gap}. Next, we have coupled the RF module to the electrostatics and solid mechanics through this nanoantenna feed gap voltage, to obtain the mechanical deflection of the two microcantilevers, as the main simulation output. On the one hand, RF simulation conditions are characterized by the definition of a lumped port or a Gaussian laser beam as excitation sources, depending on the analysed output magnitude. Thus, to obtain the S_{11} frequency response of the nanoantenna, lumped port excitation is needed, whilst a gaussian beam excitation is more convenient to calculate the feed gap voltage. Geometry characteristics and material properties used in the simulations are provided in Table 1 and Table 2, respectively. Values reported in Table 1 are mainly obtained from the microcantilevers datasheet [24], from SEM images shown in Fig. 4 and from the nanoantenna optimization to 1.55 μm wavelength process described below. Among the properties reported in Table 2, the most important, and not specified there, are the permittivity vs. wavelength ($\varepsilon_r(\lambda)$), which are inferred from [25], and correspond to Johnson and Christy (for Au) and Luke et al. (for Si_3N_4) experimental data. The simulation procedure involves constructing a 3D model of the NEMSTENNA design and considering a perfect match layer (PML) boundary condition [26] as an outer layer of the simulation box. In addition, the NEMSTENNA is surrounded by air including the gap area. Furthermore, a high mesh refinement has been taken into account in the gap area [22]. For the focused laser beam the paraxial approximation of a Gaussian beam has been used, and the laser power and beam radius are between 10 mW and 500 mW and 27.5 μm, respectively.

Table 1
Geometry dimensions of the NEMSTENNA device used in COMSOL simulations.

Parameter	Value
Dipole arm length ($L_{Arm1}/L_{Arm\ 2}$)*, μm	0.72/0.75
Dipole arm width (w_2)*, μm	0.1
Dipole length (L_1/L_2)*, μm	0.82/0.85
Dipole width (w_1)*, μm	0.1
Dipole gold thickness (t_{gd})**, μm	0.035
Dipole silicon nitride thickness (t_{dd})***, μm	0.14
Cantilever length (l_c)**, μm	200
Cantilever width (w_c)**, μm	28
Cantilever base width (w_b)**, μm	184
Cantilever spring constant (k_c)**, N/m	0.08
Cantilever silicon nitride thickness (t_{dc})**, μm	0.6
Cantilever gold thickness (t_{gc})**, μm	0.07
Capacitive gap (g_0)*, nm	10
Overlapping Area (A)*, μm^2	0.01
Dipole resonant wavelength/frequency (f_d), μm/THz	1.55/193.41

* From optimization at 1.55 μm.
** From [24].
*** From SEM images of Fig. 4.

Table 2
Material properties used in our NEMSTENNA COMSOL design and modelling.

Parameter	Air	Gold	Silicon Nitride
Young Modulus *E*, (*Pa*)	–	79×10^9	250×10^9
Poisson's ratio ν	–	0.44	0.23
Density ρ, kg/m^3	–	19,300	3100
Relative permittivity ε_r	1	$\varepsilon_r(\lambda)$	$\varepsilon_r(\lambda)$
Electrical conductivity σ, *(S/m)*	0	45.6×10^6	0

To examine the NEMSTENNA deflection in a steady-state response, the study started with the RF design module and it ended using electromechanical forces multiphysics (including coupling between solid mechanics and electrostatics physics). First, nano-antennas, located on the tip of the cantilevers, were excited using a Gaussian laser beam to generate the V_{gap} induced voltage. Then, this calculated voltage was employed as an input for the electromechanical forces multiphysics approach, integrating solid mechanics and electrostatics physics. To simulate the system, a dynamic approach was taken, utilizing a moving mesh within the simulation box that housed the NEMSTENNA in an air environment, which prevented non-convergence issues. Convergence was achieved using COMSOL segregated solver for observing stationary steady-state responses, while accounting for geometric nonlinearity in the simulation.

4.2. Optimization and tolerance analysis

4.2.1. Design of the optimum nanoantenna

Prior to the tolerance analysis, we have designed the nanoantenna to optimize S_{11} at 1.55 μm (193.41 THz). In this process, L_1, L_2, L_{Arm1}, L_{Arm2} and W_1=W_2 are taken as free parameters for optimization, while Si_3N_4 thickness is supposed to be 140 nm, as observed in SEM images of Fig. 4. The gap distance is initially fixed to $g_0 = 10$ nm. Thus, deepest S_{11} notch is achieved for $L_1 = 820$ nm, $L_2 = 850$ nm, $L_{Arm1} = 720$ nm, $L_{Arm2} = 750$ nm and $W_1 = W_2 = 100$ nm as shown in Fig. 5a (bold blue curve). It is worth to note that the nanoantenna design is not optimized in terms of receiving efficiency, since the large mismatch between the illumination spot area ($2.4{\cdot}10^{-9}$ m^2) and the nanoantenna aperture ($1.6{\cdot}10^{-13}$ m^2) implies that only the $1.6{\cdot}10^{-3}$% of the radiated power is harnessed by the nanoantenna. In future applications, such an efficiency can be improved by arraying several nanodipoles in parallel, to extend in the transversal direction the effective area of the device.

4.2.2. Tolerance analysis of the nanoantenna

Once the optimum dimensions have been found, an analysis of the fabrication tolerance effects on the S_{11} vs. frequency curves has been also carried out. In this analysis, we have considered 50 nm as an upper limit of the geometry tolerance, which is given by the resolution of the particular FIB milling process we have used. The results of this analysis are summarized in Fig. 5a. As it can be observed, if L_1 and L_2 optimum values are deviated simultaneously along the same direction by 50 nm, which corresponds to the two worst cases, the S_{11} notch is produced at 190 THz ($L_1 + 50$ nm and $L_2 + 50$ nm) or 200 THz (L_1–50 nm and L_2_50 nm), as shown in the dark cyan and gray curves in Fig. 5.a, respectively. Alternatively, if we suppose that the excitation radiation cannot be tuned to the nanoantenna resonance and its frequency is fixed to 193.41 THz, then a change in S_{11} from −22 dB (optimum L_1 and L_2) to −9 dB (L_1–50 nm and L_2–50 nm) or − 14 dB ($L_1 + 50$ nm and $L_2 + 50$ nm) will be produced at the excitation frequency.

Given the relevance of the feed gap voltage, V_{gap}, in the transduction mechanism of the NEMSTENNA, we have also analysed the fabrication tolerance effect on this magnitude. The results of this analysis are portrayed in Fig. 5b, which are obtained by taking a radiation power of 500 mW, as considered a moderately high limit of experimentally achievable laser source. As expected, we first notice that the optimum V_{gap} vs. frequency curve has its peak at the same frequency that maximizes S_{11}, i.e. the design frequency 193.41 THz. In other words, both S_{11} and V_{gap} get their maximum simultaneously. Also as expected, we find that the effect on V_{gap} of L_1 and L_2 worst case deviations is like the effect observed in S_{11}. In this case, however, voltage V_{gap} is increased to 100 mV (20 mV up from the optimum 80 mV value), which suppose an improvement, when deviation on L_1 and L_2 is in the reduction direction (L_1–50 nm and L_2–50 nm). Such an increase of V_{gap}, which does not correspond to an increase of the S_{11} notch depth, is probably produced because the matching between the dipole impedance and the free space impedance is better than the matching between the dipole impedance and the 50 Ω of the port used to calculate S_{11}. In the other worst case (L_1 + 50 nm and L_2 + 50 nm) voltage is reduced to 40 mV. From this analysis we can derive a maximum sensitivity value of $\partial V_{gap}/\partial L_{1,2} = -0.4$ mV/nm at f = 193.41 THz.

On the other hand, we have been also interested in analysing the sensitivity of V_{gap} to the Si_3N_4 layer thickness in the nanoantenna. The resulting data of this analysis are shown in Fig. 6, which are obtained for 500 mW of laser power. As it can be observed, V_{gap} is almost insensitive to Si_3N_4 thickness variations between 350 nm and 600 nm, but presents

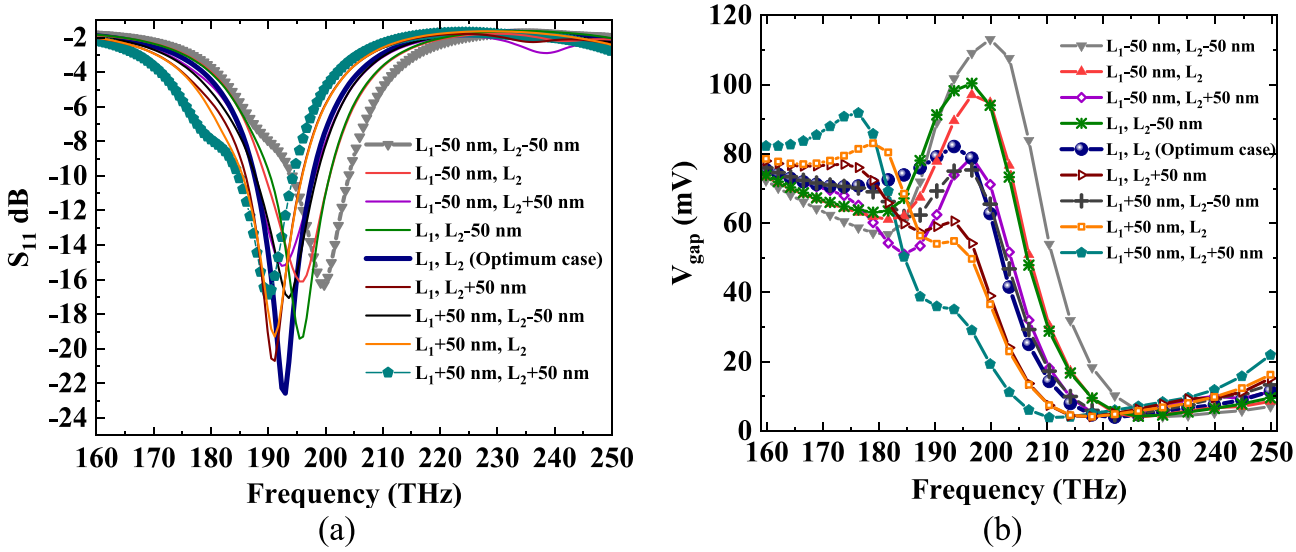

Fig. 5. Frequency response of S_{11} (a) and V_{gap} (b) obtained from COMSOL simulation, for 8 different values of L_1 and L_2 around the optimum case. Laser power is 500 mW and gap distance is $g_0 = 10$ nm.

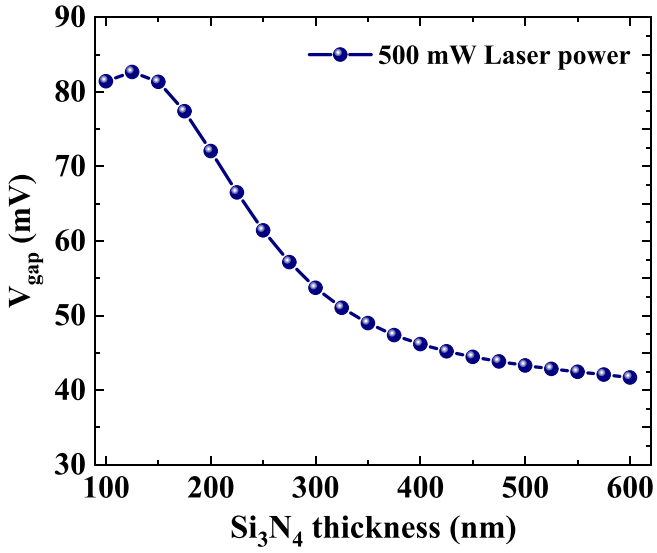

Fig. 6. V_{gap} vs Si_3N_4 thickness at 193.41 THz ($\lambda = 1.55$ μm) for a laser power of 500 mW and a gap distance of $g_0 = 10$ nm.

a maximum sensitivity of $V_{gap}/\partial t_{Si3N4} = -0.16$ mV/nm around 200 nm. On the other hand, according to the curve of Fig. 6, the optimum Si_3N_4 thickness that maximize V_{gap} is around 125 nm, which is above the lower fabrication limit of 50 nm.

4.2.3. Tolerance analysis of the NEMSTENNA opto-mechanical response

Finally, after coupling RF, electrostatics and solid mechanics modules in a multi-physics setup, we have calculated the feed gap voltage, V_{gap}, and the microcantilever deflection induced by the electrostatic force in terms of the cantilever free end displacement, for different initial gap distances and for three different laser powers: 10 mW as the maximum power achievable in our experimental setup in the DUT (Device Under Test) position, 100 mW as an intermediate value and 500 mW as the upper limit of experimentally achievable power. This calculation has been carried out for the optimum case (L_1,L_2), for the upper deviation case (L_1 + 50 nm and L_2 + 50 nm) and for the lower deviation case (L_1–50 nm and L_2–50 nm). The corresponding family of curves are shown in Fig. 7.a, Fig. 7.b and Fig. 7.c, respectively.

In accordance with the findings outlined in section 4.2.2, the application of a laser beam with a power of 0.5 W and a wavelength $\lambda = 1.55$ μm, yields a V_{gap} of 84 mV within the nanoantenna feed gap, as depicted in Fig. 7.a, for an initial gap $g_0 = 10$ nm. In these conditions, the induced free end displacement of the cantilevers is around 0.02 nm, which is unpractical since it is too close to the detectability limit. Notably, while it is apparent that in the lower deviation case (L_1–50 nm, L_2–50 nm) a higher gap voltage can be generated, 110 mV at f = 200 THz and 100 mV

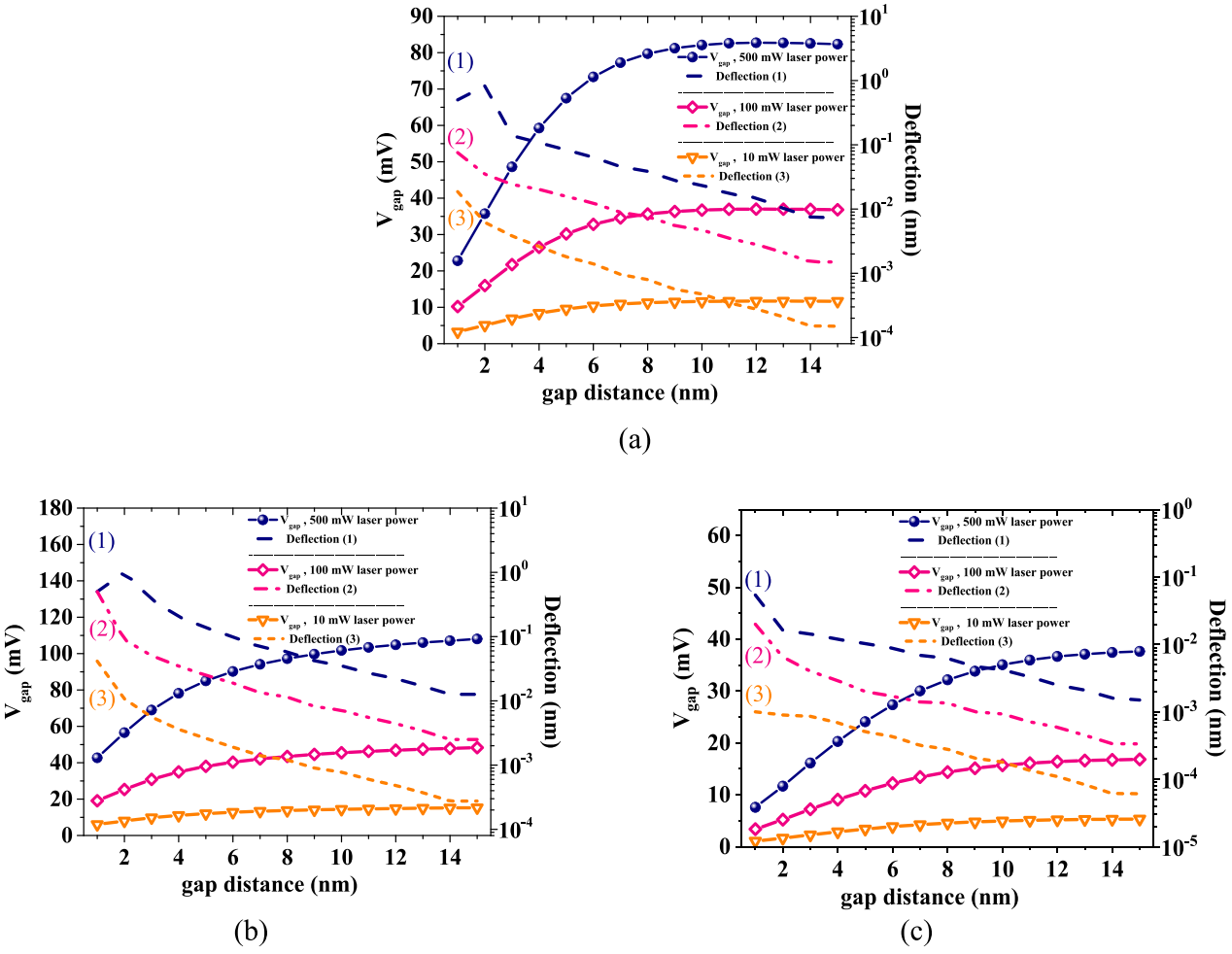

Fig. 7. Free end displacement (dashed lines referred to right y-axis) of one of the microcantilever components and gap voltage (symbol-continuous lines referred to left y-axis) as a function of the different feed gap distances of the nanoantenna for the optimum case (L_1, L_2) (a), the lower deviation case (L_1–50 nm, L_2–50 nm) (b), and the upper deviation case (L_1 + 50 nm, L_2 + 50 nm) (c) at 193.41 THz ($\lambda = 1.55$ μm), for 3 different laser power values 10, 100 and 500 mW.

at f = 193.41 THz, it cannot be considered an optimal configuration because, in comparison to the optimum case (L_1, L_2), it corresponds to a resonance frequency, in the vicinity of 200 THz, which means that it exhibits a deep notch and resonance at this higher frequency rather than the targeted 193.41 THz. Therefore, if the (L_1–50 nm, L_2–50 nm) dimensions were chosen, it would come at the cost of having a lower S_{11} value at 193.41 THz, given that the deepest notch occurs not at 193.41 THz but at a higher frequency near 200 THz. Moreover, the increase of V_{gap} obtained in the lower deviation case does not imply a significant increase on the cantilevers free end displacement, which is only grown from 0.02 nm to 0.03 nm, as it is observed in Fig. 7.b. In Fig. 7.c the results of the upper deviation case (L_1 + 50 nm, L_2 + 50 nm) are presented. In this least favourable scenario, characterized by the lowest induced voltage and a shift in resonance frequency to a lower value, approximately at 190 THz, the cantilever free end displacement is dramatically reduced to 3 pm, as illustrated in Fig. 7.c.

On the other hand, according to Eq. (3), the electrostatic force and, consequently, the induced free end cantilever displacement can be increased by reducing the initial gap distance, g_0. This trend, which can be observed in all free end cantilever displacement curves in Fig. 7, is even enhanced when pull-in conditions are achieved, as indicated by the abrupt displacement change observed for a gap distance around $g_0 = 2$ nm. In summary, if the NEMSTENNA is illuminated by a high laser power (500 mW), a detectable 0.02–0.03 nm cantilever free end displacement can be induced for an initial gap distance of $g_0 = 10$ nm, in both the optimum and lower deviation cases. This displacement is reduced to a fully unpractical 3 pm in the upper deviation case. However, even in this least scenario, a reduction of the initial gap to $g_0 = 2$ nm or below produces an increase of the cantilever free end displacement up to 0.1 nm, that reaches up to 1 nm in the most favourable cases. Note that in such cases, the displacement for an initial gap $g_0 = 2$ nm is limited to 1 nm by the collapse of the cantilevers produced by the pull-in effect. Similarly, for an initial gap $g_0 = 1$ nm the displacement is limited to 0.5 nm.

On the contrary, if the laser power is at the level of our current experimental setup (10 mW), then only the optimum and lower deviation cases would reach a displacement over 0.01 nm when the initial gap has the most favourable value of $g_0 = 2$ nm. It is worth to notice that, in practice, the gap distance in the feed gap area of the nanoantenna can be adjusted and controlled with a resolution below 1 nm using a state-of-the-art 3D nanopositioner, that can even allow the tuning of the overlapping distance too.

5. Conclusions

In conclusion, our study explores a novel device that directly converts near-infrared optical radiation into mechanical motion. Utilizing a plasmonic optical nanoantenna integrated within a microcantilever, we demonstrate a feasible fabrication process using Focused Ion Beam (FIB) milling. Our analysis reveals the sensitivity of device characteristics to fabrication tolerances, expanding the MEMSTENNA concept into the near-infrared range. The effect of the excitation power, the Si_3N_4 thickness and the feed gap distance on the NEMSTENNA mechanical response in terms of cantilevers deflection has been analysed. A mechanical response of 0.01–0.1 nm, which is clearly inside the detectability range, makes the designed NEMSTENNA for 1.55 μm appropriate as a proof of concept demonstrator, but unsuitable for practical purposes. Thus, a refinement of the NEMSTENNA design is still needed. This innovative device offers remote actuation through the conversion of electromagnetic signals into mechanical movement, presenting a promising avenue for energy-efficient applications in opto-mechanical systems which could be investigated in upcoming research.

Declaration of competing interest

The authors declare that they have no known competing financial interest or personal relationships that could have appeared to influence the work reported in this paper.

Data availability

Data will be made available on request.

Acknowledgements

This work was funded by Spain's Ministerio de Ciencia e Innovación under Grant No. PID2021-127840NB-I00 (MICINN/AEI/FEDER, UE).

References

[1] R. Ruiz, G. Abadal, Direct transduction from radiofrequency radiated power to static and dynamic flexural mechanical modes, in: 2021 21st Int. Conf. Solid-State Sensors, Actuators Microsystems, 2021, pp. 144–147, https://doi.org/10.1109/Transducers50396.2021.9495668.
[2] R. Ruiz, J. Bonache, G. Abadal, A flexible dipole antenna for direct transduction of microwave radiated power into DC mechanical deflection, Sensors Actuators A Phys. 340 (2022) 113536, https://doi.org/10.1016/j.sna.2022.113536.
[3] R. Ruiz, G. Abadal, Remote dynamic actuation of an electrostatically driven microcantilever by a wireless power transfer system, Sensors Actuators A Phys. 345 (2022) 113798, https://doi.org/10.1016/j.sna.2022.113798.
[4] C. Belacel, Y. Todorov, S. Barbieri, D. Gacemi, I. Favero, C. Sirtori, Optomechanical terahertz detection with single meta-atom resonator, Nat. Commun. 8 (2017) 1578, https://doi.org/10.1038/s41467-017-01840-6.
[5] C. Li, Y. Zhang, K. Hirakawa, Terahertz detectors using microelectromechanical system resonators, Sensors (Basel) 23 (2023), https://doi.org/10.3390/s23135938.
[6] H. Zhu, K. Wang, G. Liu, G. Wang, J. Mou, W. Zhang, G. Wei, A terahertz optomechanical detector based on metasurface and bi-material micro-cantilevers, Micromachines 13 (2022), https://doi.org/10.3390/mi13050805.
[7] J. Liu, B. Chomet, P. Beoletto, D. Gacemi, K. Pantzas, G. Beaudoin, I. Sagnes, A. Vasanelli, C. Sirtori, Y. Todorov, Ultrafast detection of TeraHertz radiation with miniaturized optomechanical resonator driven by dielectric driving force, ACS Photonics 9 (2022) 1541–1546, https://doi.org/10.1021/acsphotonics.2c00227.
[8] A. Ashkin, Trapping of atoms by resonance radiation pressure, Phys. Rev. Lett. 40 (1978) 729–732, https://doi.org/10.1103/PhysRevLett.40.729.
[9] M. Dykman, Heating and cooling of local and quasilocal vibrations by a nonresonance field, Sov. Phys. Solid State 20 (1978) 1306–1311.
[10] S. Gröblacher, J.B. Hertzberg, M.R. Vanner, G.D. Cole, S. Gigan, K.C. Schwab, M. Aspelmeyer, Demonstration of an ultracold micro-optomechanical oscillator in a cryogenic cavity, Nat. Phys. 5 (2009) 485–488, https://doi.org/10.1038/nphys1301.
[11] E. Verhagen, S. Deléglise, S. Weis, A. Schliesser, T.J. Kippenberg, Quantum-coherent coupling of a mechanical oscillator to an optical cavity mode, Nature 482 (2012) 63–67, https://doi.org/10.1038/nature10787.
[12] J. Chan, T.P.M. Alegre, A.H. Safavi-Naeini, J.T. Hill, A. Krause, S. Gröblacher, M. Aspelmeyer, O. Painter, Laser cooling of a nanomechanical oscillator into its quantum ground state, Nature 478 (2011) 89–92, https://doi.org/10.1038/nature10461.
[13] C. Fumeaux, J. Alda, G.D. Boreman, Lithographic antennas at visible frequencies, Opt. Lett. 24 (1999) 1629–1631, https://doi.org/10.1364/ol.24.001629.
[14] A.E. Krasnok, I.S. Maksymov, A.I. Denisyuk, P.A. Belov, A.E. Miroshnichenko, C. R. Simovski, Y.S. Kivshar, Optical nanoantennas, Physics-Uspekhi. 56 (2013) 539, https://doi.org/10.3367/UFNe.0183.201306a.0561.
[15] F.J. Gonzalez, B. Ilic, J. Alda, G.D. Boreman, Antenna-coupled infrared detectors for imaging applications, IEEE J. Sel. Top. Quantum Electron. 11 (2005) 117–120, https://doi.org/10.1109/JSTQE.2004.841474.
[16] E. Briones, J. Alda, F.J. González, Conversion efficiency of broad-band rectennas for solar energy harvesting applications, Opt. Express 21 (2013) A412–A418, https://doi.org/10.1364/OE.21.00A412.
[17] Z. Zhu, S. Joshi, B. Pelz, G. Moddel, Overview of optical rectennas for solar energy harvesting, in: O.V. Sulima, G. Conibeer (Eds.), Next Gener. Photonic Cell Technol. Sol. Energy Convers. IV, 2013, p. 88240O, https://doi.org/10.1117/12.2024700.
[18] Z. Ma, G.A.E. Vandenbosch, Optimal solar energy harvesting efficiency of nano-rectenna systems, Sol. Energy 88 (2013) 163–174, https://doi.org/10.1016/j.solener.2012.11.023.
[19] J. Alda, C. Fumeaux, M.A. Gritz, D. Spencer, G.D. Boreman, Responsivity of infrared antenna-coupled microbolometers for air-side and substrate-side illumination, Infrared Phys. Technol. 41 (2000) 1–9, https://doi.org/10.1016/S1350-4495(99)00036-5.
[20] C. Di Garbo, P. Livreri, G. Vitale, Optimal matching between optical rectennas and harvester circuits, in: 2017 IEEE Int. Conf. Environ. Electr. Eng. 2017 IEEE Ind. Commer. Power Syst. Eur. (EEEIC / I&CPS Eur), 2017, pp. 1–6, https://doi.org/10.1109/EEEIC.2017.7977686.
[21] J. Dorfmüller, R. Vogelgesang, W. Khunsin, C. Rockstuhl, C. Etrich, K. Kern, Plasmonic nanowire antennas: experiment, simulation, and theory, Nano Lett. 10 (2010) 3596–3603, https://doi.org/10.1021/nl101921y.
[22] J.-S. Huang, T. Feichtner, P. Biagioni, B. Hecht, Impedance matching and emission properties of Nanoantennas in an optical Nanocircuit, Nano Lett. 9 (2009) 1897–1902, https://doi.org/10.1021/nl803902t.

[23] R. Stoneback, The dipole impedance of an aperture, Prog. Electromagn. Res. B 26 (2010) 401–423, https://doi.org/10.2528/PIERB10062406.
[24] https://www.nanoandmore.com/AFM-Probe-PNP-TR-TL-Au, 2024.
[25] M.N. Polyanskiy, Refractive Index Database, 2024.
[26] Z. Ma, G.A.E. Vandenbosch, Input impedance of optical metallic nano dipole over 300 nm – 1200 nm wavelength, in: 2013 7th Eur. Conf. Antennas Propag, 2013, pp. 3810–3813.